OPEN ACCESS



VLBA Astrometry of the Galactic Double Neutron Stars PSR J0509+3801 and PSR J1930–1852: A Preliminary Transverse Velocity Distribution of Double Neutron Stars and its Implications

Hao Ding ^{1,8}, Adam T. Deller ², Joseph K. Swiggum ^{3,4}, Ryan S. Lynch ⁵, Shami Chatterjee ⁶, and Thomas M. Tauris ⁷, Mizusawa VLBI Observatory, National Astronomical Observatory of Japan, 2-12 Hoshigaoka-cho, Mizusawa, Oshu, Iwate 023-0861, Japan ² Centre for Astrophysics & Supercomputing, Swinburne University of Technology, P.O. Box 218, Hawthorn, Victoria 3122, Australia ³ Center for Gravitation, Cosmology, and Astrophysics, Department of Physics, University of Wisconsin–Milwaukee, P.O. Box 413, Milwaukee, WI 53201, USA ⁴ Department of Physics, 730 High St., Lafayette College, Easton, PA 18042, USA ⁵ Green Bank Observatory, PO Box 2, Green Bank, WV 24944, USA ⁶ Cornell Center for Astrophysics and Planetary Science, Ithaca, NY 14853, USA ⁷ Department of Materials and Production, Aalborg University, DK-9220 Aalborg Øst, Denmark Received 2024 March 27; revised 2024 May 5; accepted 2024 May 6; published 2024 July 18

Abstract

The mergers of double neutron star (DNS) systems are believed to drive the majority of short γ -ray bursts (SGRBs), while also serving as production sites of heavy r-process elements. Despite being key to (i) confirming the nature of the extragalactic SGRBs, (ii) addressing the poorly understood r-process enrichment in the ultrafaint dwarf galaxies (UFDGs), and (iii) probing the formation process of DNS systems, the space velocity distribution of DNSs is still poorly constrained, due to the small number of DNSs with well-determined astrometry. In this work, we determine new proper motions and parallaxes of two Galactic DNSs, PSR J0509+3801 and PSR J1930-1852, using the Very Long Baseline Array, and we estimate the transverse velocities v_{\perp} of all 11 isolated Galactic DNSs having proper-motion measurements in a consistent manner. Our correlation analysis reveals that the DNS v_{\perp} is tentatively correlated with three parameters: spin period, orbital eccentricity, and companion mass. With the preliminary v_{\perp} distribution, we obtain the following findings. First, the refined v_{\perp} distribution is confirmed to agree with the observed displacements of the localized SGRBs from their host galaxy birth sites. Second, we estimate that around 11% and 25% of DNSs remain gravitationally bound to UFDGs with escape velocities of 15 and 25 km s⁻¹, respectively. Hence, the retained DNSs might indeed be responsible for the r-process enrichment confirmed so far in a few UFDGs. Finally, we discuss how a future ensemble of astrometrically determined DNSs may probe the multimodality of the v_{\perp} distribution.

Unified Astronomy Thesaurus concepts: Very long baseline interferometry (1769); Radio pulsars (1353); Proper motions (1295); Annual parallax (42)

1. Introduction

1.1. Pulsars in Double Neutron Star Systems

Double neutron stars (DNSs) are valuable "laboratories" for probing theories of gravity, close binary star evolution, and supernovae (SNe) and unveiling the composition of neutron stars (NSs). The gravitational-wave (GW) detection of the DNS merger event GW170817 (Abbott et al. 2017a), in conjunction with extensive observations across the electromagnetic spectrum (e.g., Abbott et al. 2017b; Mooley et al. 2018), has offered rich insights into the NS interior (Annala et al. 2018). A short γ -ray burst (SGRB; Goldstein et al. 2017) coincident with the GW170817 merger event supports the widely believed association between DNS mergers and SGRBs (e.g., Fox et al. 2005; Coward et al. 2012; Fong et al. 2022; O'Connor et al. 2022), although most identified SGRBs are beyond the horizon of current GW detectors. Additionally, light-curve monitoring and analysis after the GW170817 event suggest that heavy elements were produced during the DNS merger (Drout et al. 2017; Watson et al. 2019),

Original content from this work may be used under the terms of the Creative Commons Attribution 4.0 licence. Any further distribution of this work must maintain attribution to the author(s) and the title of the work, journal citation and DOI.

which reinforces the belief that DNS mergers are a prime source of *r*-process elements (Eichler et al. 1989; Korobkin et al. 2012). Nonetheless, it remains uncertain whether DNS mergers dominate the production of *r*-process elements.

Before the violent merger of a DNS is the phase of steady inspiraling. In this phase, Galactic DNSs that host an observable pulsar (hereafter referred to as DNS pulsars) have been extensively studied (e.g., Hulse & Taylor 1975; Stairs et al. 2002; Faulkner et al. 2005; Jacoby et al. 2006; Kramer et al. 2006; Cameron et al. 2018; Stovall et al. 2018) with pulsar timing, a technique that measures and models the pulse times of arrival from a pulsar. Despite being in shallower gravitational potentials compared to DNS mergers, DNS pulsars have offered some of the most stringent tests on gravitational theories in the strong-field regime with long-term timing observations (e.g., Fonseca et al. 2014; Wex 2014; Weisberg & Huang 2016; Ferdman et al. 2020; Kramer et al. 2021a). These tests are made by comparing observed post-Keplerian (PK) parameters, which quantify effects beyond a simple Keplerian model of motion, to the predictions of a specific gravitational theory, e.g., the general theory of relativity.

There are two distinct channels of DNS formation: the predominant "isolated" channel, and the "dynamical" channel (see Tauris & van den Heuvel 2023 and references therein). The former channel gives rise to field DNSs, namely DNS systems born in isolated environments, while both channels can

⁸ EACOA Fellow.

occur in dense regions such as globular clusters (Zevin et al. 2019). At the time of writing, only 19 known DNS pulsars and 2 suspected ones have been discovered from pulsar surveys (Sengar et al. 2022), including two found in globular clusters.

1.2. Probing the Kinematics of Field DNSs with Precise Astrometry

Precise proper-motion and distance measurements for Galactic DNSs are essential for the studies related to DNSs. The orbital period derivative \dot{P}_b (or orbital decay) of a DNS system measured by pulsar timing is a PK parameter biased by the Shklovskii effect (Shklovskii 1970), an apparent acceleration due to the pulsar's transverse motion. \dot{P}_b is also affected by the radial acceleration caused by the overall gravity of the Galaxy (see Zhu et al. 2019 and references therein); this acceleration depends on our distance to the pulsar. Correcting the measured values for these effects requires an accurate measurement of the distance and proper motion. As the precision of the observed orbital decay \dot{P}_b^{obs} improves as $t^{-2.5}$ (where t refers to the observing time), the uncertain Shklovskii contribution to \dot{P}_b can quickly become the limiting factor of the \dot{P}_b test on gravitational theories (e.g., Deller et al. 2018; Ding et al. 2021).

Collectively, the measurements of DNS proper motions and distances allow a sample study of space velocities (also known as peculiar velocities or systemic velocities) of DNSs, which, combined with a DNS delay time distribution and galactic gravitational potentials, can be used to predict the spatial distribution of DNS merger sites within, or nearby, a host galaxy (e.g., Bloom et al. 1999; Voss & Tauris 2003; Fong & Berger 2013; Beniamini & Piran 2016, 2019; Tauris et al. 2017; Vigna-Gómez et al. 2018; Andrews & Zezas 2019; Zevin et al. 2022). Such a prediction, once made, can be compared to DNS mergers (Abbott et al. 2017b) and SGRBs localized with respect to their host galaxies, in order to probe the poorly defined selection biases (on both sides of the comparison) and identify exotic transient events. Most pinpointed SGRBs are found far from the centers of their host galaxies and starforming regions (e.g., Fox et al. 2005; Fong & Berger 2013; Tunnicliffe et al. 2014; Fong et al. 2022; O'Connor et al. 2022). Assuming that SGRBs are predominantly generated by DNS mergers, the transverse space velocities v_{\perp}^{SGRB} of $\approx 20-140 \text{ km s}^{-1}$ with a median of $\approx 60 \text{ km s}^{-1}$ were inferred from the SGRB displacements from their expected birth sites (Fong & Berger 2013), in conjunction with the indicative DNS delay time estimated by Leibler & Berger (2010). On the other hand, as the direct link between SGRB localizations and DNS formation theories, the space velocities of Galactic DNSs have been previously investigated with ≤9 proper-motion and distance measurements (Wong et al. 2010; Tauris et al. 2017; Haniewicz et al. 2021): the preliminary observational constraints suggest overall consistency with v_{\parallel}^{SGRB} .

Furthermore, a space velocity distribution of DNSs is crucial for understanding the source of excess r-process elements in ultrafaint dwarf galaxies (UFDGs; Ji et al. 2016; Hansen et al. 2017, 2020), where the escape velocities (\sim 15 km s $^{-1}$) can be easily surpassed owing to the NS natal kicks received at SNe (Beniamini et al. 2016; Safarzadeh et al. 2019). On the other hand, if a considerable fraction (e.g., \gtrsim 10%) of DNSs have a space velocity of \leqslant 15 km s $^{-1}$, then it is plausible that the r-process elements detected in UFDGs came from DNS mergers bound by the gravity of the host UFDGs. Otherwise, the r-process elements in UFDGs must be produced through

fast-merging DNSs (Safarzadeh et al. 2019) or other mechanisms.

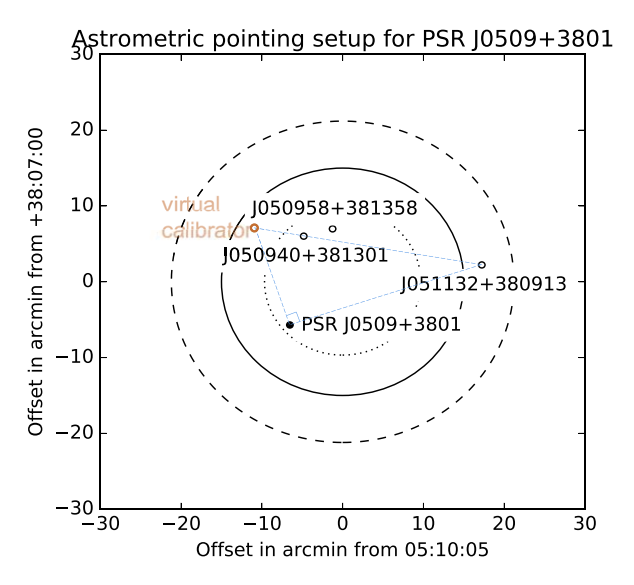
Finally, the DNS formation is not yet fully understood: for example, it remains debated under which conditions an electroncapture SN (ECSN), instead of a conventional iron core-collapse SN (CCSN), can give rise to the second-born NS (e.g., Podsiadlowski et al. 2004, 2005; Knigge et al. 2011; Jones et al. 2016; Giacobbo & Mapelli 2019; Tauris & Janka 2019). As ECSNe are expected to give smaller natal kicks than CCSNe (e.g., Dessart et al. 2006; Kitaura et al. 2006; Gessner & Janka 2018), DNS space velocities can be used to probe the formation channels of field DNSs. Specifically, if both the CCSN and ECSN channels contribute to the field DNS productions, one would likely find a bimodal feature in the DNS space velocity distribution. However, the picture is more blurred because (i) the narrow progenitor mass range leading to ECSNe depends on metallicity (Podsiadlowski et al. 2004; Siess & Lebreuilly 2018), and UFDGs are very metalpoor (Fu et al. 2023); and (ii) ultrastripped SNe (Tauris et al. 2013, 2015), occurring when the last-formed NS is produced in DNS progenitor systems, may also produce NSs with small kicks in both CCSNe and ECSNe (e.g., Tauris et al. 2017; Müller et al. 2019). Additionally, a positive correlation has been proposed between the second-born NS masses and SN kick magnitudes, and thus space velocities, of DNSs (Tauris et al. 2017; Burrows et al. 2023), and possibly also between second-born NS masses and orbital eccentricities, which can also be examined with more proper-motion and distance measurements of field DNSs.

Pulsar timing and very long baseline interferometry (VLBI) astrometry can provide both high-precision proper motions and potentially distances for DNSs. However, the lower timing precision attainable for the moderately recycled pulsars typically found in DNS systems (compared to fully recycled "millisecond" pulsars with periods of $\lesssim 10$ ms) means that long campaigns—often 10+ yr—are required to detect proper motion and annual geometric parallax with adequate precision. VLBI astrometry, on the other hand, generally only requires two well-separated observations to detect a high-precision proper motion, and O(10) observations over a 1 yr (or longer) span to measure annual geometric parallax with a precision of tens of microarcseconds, irrespective of the pulse period.

To date, only five DNSs have been well measured astrometrically with VLBI (Kirsten et al. 2014; Deller et al. 2018; Ding et al. 2021, 2023b; Kramer et al. 2021a), including four field DNSs (i.e., PSRB1913+16, PSR B1534+12, PSR J0737-3039A/B, and PSR J1518+4904) and a DNS in the globular cluster M15. In this work, we carried out VLBI astrometry on two field DNSs-PSR J0509+3801 and PSR J1930-1852 (see Section 6 for their introductions). In Sections 2–4, we describe the VLBI observation strategy and data reduction procedures. In particular, a novel astrometric tactic utilizing multiple reference sources is introduced in Section 3.1. We present the calculation of distances and transverse space velocities for 11 field DNSs in Section 5. The obtained sample of transverse space velocities is discussed thoroughly in Section 7, while individual DNS systems are discussed in Section 6. Throughout this paper, uncertainties are provided at 68% confidence, unless otherwise stated.

2. Observations

For both PSR J0509+3801 and PSR J1930-1852, we made a total of eight observations with the Very Long Baseline Array (VLBA) in the period 2015 March-2016 November under the



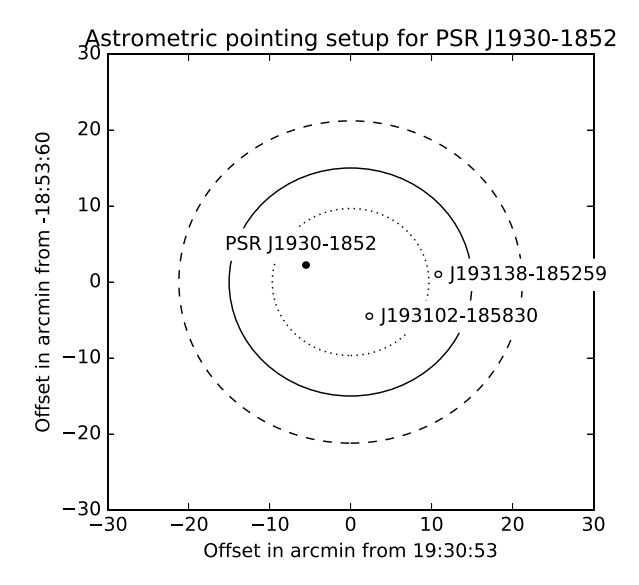


Figure 1. The locations of the target pulsar and the background calibrator sources within the VLBA primary beam. The 75%, 50%, and 25% beam response levels are plotted with dotted, solid, and dashed lines, respectively. NVSS J193138–185258 is used as the phase reference source for PSR J1930–1852. The astrometry of PSR J0509+3801 is carried out using the novel 2X (read as "two cross") strategy (see Section 3.1 for more explanations), where the virtual calibrator illustrated as the orange circle is used alongside the primary in-beam calibrator NVSS J051132+380913. The virtual calibrator should lie on the line that connects the primary in-beam calibrator NVSS J050940+381301 and form a 90° angle with NVSS J051132+380913 at the position of PSR J0509+3801. Accordingly, the virtual calibrator is a factor of 1.27 farther away from NVSS J051132+380913 compared to NVSS J050940+381301.

Table 1
Observed Sources

Source Type	Source Name	$S_{1.4}^{a}$ (mJy beam ⁻¹)	Separation ^b (arcmin)	
Target	PSR J0509+3801	0.16	0	
Off-beam calibrator	ICRF J050905.8+352817	174.4	153.1	
In-beam calibrator	NVSS J051132+380913	12.1	25.1	
In-beam calibrator	NVSS J050940+381301	4.9	11.9	
In-beam calibrator	NVSS J050958+381358	2.5	13.8	
Target	PSR J1930-1852	0.12	0	
Off-beam calibrator	ICRF J192809.1-203543	99.0	109.1	
In-beam calibrator	NVSS J193138-185258	29.9	16.4	
In-beam calibrator	NVSS J193102-185830	11.0	10.3	

Notes

project code BD186. In each observation, we nodded between the target field (containing the pulsar and one or more extragalactic sources used as "in-beam" calibrators) and a nearby gain and delay calibrator source. The locations of the pulsars and the background calibrator sources are shown in Figure 1. We also included two scans on a bright fringe-finder source, used to calibrate the instrumental bandpass. Each observation lasted 4 hr, with approximately 2.7 hr spent on the target field. The target sources and their corresponding calibrators are listed in Table 1.

The instrumental setup used a standard continuum setup for the 20 cm band, with eight subbands of width 32 MHz recorded in dual circular polarization at 2-bit precision for a total data rate of 2 Gbps per antenna. Within the frequency tuning limitations afforded by the VLBA's wideband recording system, we attempted to avoid regions of frequency space known to contain strong radio frequency interference at VLBA stations and selected subbands in the range 1392–1748 MHz.

The first two observations of PSR J1930-1852 yielded only weak detections, leading us to conclude both that the catalog flux density for this pulsar was overestimated and that its spectral index was steeper than expected. Accordingly, for the third observation of PSR J1930-1852 onward, we changed observing frequencies to span the range 1252-1508 MHz. We note that this change is likely to cause a small (if not negligible) reference point offset for the first two observations of PSR J1930-1852, due to the frequency-dependent core shift (e.g., Voitsik et al. 2018) of the in-beam calibrator NVSS J193138-185258, and potentially lead to a slightly larger scaling factor $\eta_{\rm EFAC}$ of the fiducial systematic errors in the astrometry inference (see Section 4). Data were correlated using the VLBA DiFX correlator (Deller et al. 2011), making use of pulsar gating to improve the signal-to-noise ratio on the target pulsars. For the pulsar gating, we adopted the pulse ephemerides acquired from pulsar timing observations using the Green Bank Telescope.

^a Unresolved flux intensity (median period-averaged flux density in the case of the pulsars) at 1.4 GHz.

^b Angular separation from the target pulsar.

3. Data Reduction

We make use of the ParselTongue/AIPS (Greisen 2003; Kettenis et al. 2006) astrometric reduction pipeline psrvlbireduce described in Deller et al. (2016) and Ding et al. (2023b), and here we briefly summarize the main steps. A priori amplitude calibration including correction for the primary beam response is followed by time-independent delay and bandpass calibration using the fringe-finder source, and then by time-dependent delay and gain calibration using the out-of-beam calibrator. The calibrator source models used in these steps, as well as in the phase calibration refinement that follows, were derived from a concatenated data set that included all eight observations and have been made available online¹⁰ to facilitate reproduction of our data reduction results. The cumulative calibration derived so far is then applied to the sources in the target field (the target pulsar and the in-beam calibrators), and the calibrated data sets are split and averaged in frequency.

3.1. The "2X" Tactic: Doubling the Position Measurements with Two Near-field Calibrators in Perpendicular Directions

The in-beam calibrator data have been used to refine the phase calibration for the target source, eliminating temporal interpolation along with reducing spatial interpolation of calibrator solutions. In a normal procedure, self-calibration is performed on one or sometimes multiple in-beam calibrator sources (e.g., Deller et al. 2019); the acquired solutions are then applied to all sources in the target field. The multisource selfcalibration technique (Middelberg et al. 2013; Radcliffe et al. 2016) is especially useful when all in-beam calibrators are slightly too faint for self-calibration. On the other hand, in the opposite scenario, where at least two in-beam calibrators are bright enough for self-calibration (or, alternatively, at least two relatively faint in-beam calibrators are identified around a sufficiently bright target; see, e.g., Section 4.1.2 of Ding et al. 2023b), it is possible to further enhance the astrometric precision by doubling the number of relative position measurements. Specifically, self-calibration solutions can be derived independently on each sufficiently bright in-beam calibrator. As the self-calibration solutions are applied to the target, the position of the target is measured with respect to the in-beam calibrator. Namely, one target position can be measured with respect to each independently calibrated inbeam calibrator.

However, systematic errors in the position offsets measured against different in-beam calibrators are generally at least partially correlated, due to the predominance of direction-dependent calibration errors in the systematic error budget. As an extreme and straightforward example, two in-beam calibrators situated at the same sky position would render almost perfectly correlated self-calibration solutions. Assuming that direction-dependent terms dominate the self-calibration solutions and that these terms change linearly with the sky position of the in-beam calibrator, the solutions obtained with two in-beam calibrators are largely independent of each other only when the two in-beam calibrators are in perpendicular directions as viewed from the target (and even in this case, other sources of systematic error, such as variations taking

place between adjacent calibration solutions, remain correlated). Such a pair of in-beam calibrators are hereafter referred to as orthogonal in-beam calibrators, or simply orthogonal calibrators. The chance of having a pair of physical orthogonal in-beam calibrators is rather small. However, with the help of the 1D interpolation technique (e.g., Fomalont & Kopeikin 2003; Doi et al. 2006; Ding et al. 2020b), the target can be measured with respect to a virtual calibrator (see Ding et al. 2020b for more explanations), whose effective position can be manipulated (either along the line connecting two selfcalibratable in-beam calibrators or along the line connecting the out-of-beam main phase calibrator and a self-calibratable in-beam calibrator) to form an orthogonal in-beam calibrator pair with a physical in-beam calibrator. For brevity, we hereafter refer to this novel strategy of VLBI astrometry as the 2X (read as "two cross") strategy.

Interestingly, both DNSs possess at least two self-calibratable inbeam calibrators (see Table 1). Therefore, the 2X strategy is potentially applicable to the astrometry of both DNSs. Based on the brightness and compactness of the in-beam calibrators, as well as their angular distances from the target, we adopted NVSS J051132 +380913 and NVSS J193138-185258 as the primary in-beam calibrators for PSR J0509+3801 and PSR J1930-1852, respectively. In-beam calibrators other than the primary in-beam calibrators are referred to as secondary in-beam calibrators. Unfortunately, both NVSS J050958+381358 and NVSS J193102 -185830 display a resolved jet feature in the R.A. direction. Any time dependence to the jet brightness profile along the jet direction may corrupt the parallax measurement (e.g., Deller et al. 2013), given that the parallax signature of either DNS is predominantly revealed in the R.A. direction. In such a case, the systematic error budget captured by the self-calibration solution might no longer be dominated by direction-dependent effects, breaking the underlying assumption of the 2X calibration strategy. Therefore, NVSS J050958+381358 and NVSS J193102-185830 are not used as secondary in-beam calibrators. Accordingly, we only implemented the 2X tactic on PSR J0509+3801 with its primary in-beam calibrator NVSS J051132+380913 and the secondary in-beam calibrator NVSS J050940+381301.

For each DNS, self-calibration was first performed on the primary in-beam calibrator; the acquired solutions were applied to all sources in the target field. In this way, the target position is measured with respect to the primary in-beam calibrator. After the application of in-beam phase calibration solutions to all target-field sources, we imaged both the target sources and the in-beam calibrator sources after dividing by the calibrator source model using natural weighting. From each image per source per epoch, we extracted a position and uncertainty using the image-plane fitting task JMFIT in AIPS. The positions so obtained are essentially anchored to the primary in-beam calibrator.

For PSR J0509+3801 only, we went one step further in order to fulfill the 2X strategy: this time PSR J0509+3801 needs to be phase-referenced to a virtual calibrator that forms orthogonal calibrators with the primary in-beam calibrator NVSS J051132 +380913. In practice, we implemented 1D interpolation along the line connecting the NVSS J051132+380913 and NVSS J050940 +381301 (see Ding et al. 2020b for the detailed procedure) and then applied the solutions to only PSR J0509+3801. By placing the virtual calibrator 1.27 times farther away from NVSS J051132 +380913 compared to NVSS J050940+381301, the virtual calibrator and NVSS J051132+380913 form an orthogonal pair

⁹ https://github.com/dingswin/psrvlbireduce

Available on Zenodo under an open-source Creative Commons Attribution license: doi:10.5281/zenodo.11114889

around PSR J0509+3801 (see Figure 1). In this instance, the virtual calibrator is farther away from PSR J0509+3801 than NVSS J050940+381301 (which may not be the case given a calibrator plan of another target); this means that the systematic errors (of the target positions) resulting from direction-dependent propagation effects are accordingly amplified. Despite this small setback, the overall astrometric precision is expected to be improved (see Section 4).

4. The Inference of Astrometric Parameters

After the VLBI data reduction (see Section 3), we compiled the positions of PSR J0509+3801 and PSR J1930-1852 across all epochs, which are made available (see footnote 10) as the "pmpar.in.preliminary" files. For PSR J1930–1852, one series of positions was measured with respect to the primary in-beam calibrator NVSS J193138-185258, while two position series were acquired for PSR J1930-1852 against two different inbeam calibrators, as the 2X strategy had been applied (see Section 3.1). The uncertainties of these target positions only reflect the thermal noise in the target images. On top of the random positional errors, we estimated systematic uncertainties using an empirical estimator (Equation (1) of Deller et al. 2019) based on the angular separation of the calibrator and target (taking the fiducial value as explained in Section 3 of Ding et al. 2023b) and added them in quadrature to the random errors. The full positional uncertainties are provided online (see footnote 10) in the "pmpar.in" files.

Following Ding et al. (2023b), we inferred the astrometric parameters of the two DNSs using the astrometric Bayesian inference package $sterne.py^{11}$ (Ding et al. 2021). The revealed parallax signatures are illustrated in Figure 2. The inferred values are presented in Table 2, while the corner plots of the inferences are available online (see footnote 10). Among the parameters of inference, $\eta_{\rm EFAC}$ is the scaling factor on the fiducial systematic error (see Equation (1) of Ding et al. 2023b); i_{orb} and Ω_{orb} stand for orbital inclination angle and the ascending node longitude, respectively. As the detectability of orbital motion with VLBI, quantified by η_{orb} defined with Equation (3) of Ding et al. (2023b), is very low ($\eta_{orb} = 0.03$, as compared to 1) for PSR J0509+3801, we only inferred i_{orb} and $\Omega_{\rm orb}$ (on top of other astrometric parameters) for PSR J1930 -1852 (with $\eta_{orb} = 1.1$). Nevertheless, without useful prior knowledge of either orbital parameter, we did not achieve nontrivial constraints on $i_{\rm orb}$ and $\Omega_{\rm orb}$ of PSR J1930–1852 (see Table 2 and the online corner plot (see footnote 10)).

4.1. The Absolute Reference Positions of PSR J0509+3801 and PSR J1930-1852

We estimated the absolute reference positions of PSR J0509+3801 and PSR J1930-1852 in the same way as described in Section 3.2 of Ding et al. (2020a), except that, instead of the bootstrap uncertainties of the relative reference positions with respect to the primary in-beam calibrator, the Bayesian ones were adopted here as part of the error budget of the absolute reference positions. At the reference epoch MJD 57381, the absolute position of PSR J0509+3801 is $\alpha_{\text{J0509+3801}} = 05^{\text{h}}09^{\text{m}}31.78871 \pm 0.4 \,\text{mas} \pm 0.8 \,\text{mas}, \, \delta_{\text{J0509+3801}} = +38^{\circ}01'18.'' \,0730 \pm 0.6 \,\text{mas} \pm 0.8 \,\text{mas}, \, \text{while the absolute position of PSR J1930-1852}$ is

 $\alpha_{\rm J1930-1852} = 19^{\rm h}30^{\rm m}29^{\rm s}.7156 \pm 2.2$ mas ± 0.8 mas, $\delta_{\rm J1930-1852} = -18^{\circ}51'46''.$ 164 ± 8.1 mas ± 0.8 mas at MJD 57433. For both positions, the second error terms are indicative of the frequency-dependent core shift of the off-beam phase calibrator (Sokolovsky et al. 2011; see also the explanation in Section 3.2 of Ding et al. 2020a); the first error terms consist of (1) the Bayesian uncertainty of the relative reference position measured with respect to the primary in-beam calibrator, (2) the position scatter of the primary in-beam calibrator (across all epochs) with respect to the off-beam phase calibrator, and (3) the uncertainty of the off-beam phase calibrator position routinely updated in the Radio Fundamental Catalog. 12

5. Distances and Space Velocities

The astrometric determination of PSR J0509+3801 and PSR J1930-1852 considerably enriches the small sample of astrometrically studied field (i.e., not bound by a stellar cluster) DNSs. So far, proper-motion constraints have been reported for only 12 field DNSs (including the newly added PSR J0509 +3801 and PSR J1930-1852), which are summarized in Table 3. Among them, six DNSs also have parallax-based distance estimates (see the upper block of Table 3). In Table 3, we also provide useful information such as the Galactic longitudes l, Galactic latitudes b, spin periods P_s , orbital periods P_b , and orbital eccentricities e for the 12 DNSs, which were acquired from the PSRCAT catalog 13 (Manchester et al. 2005). Besides, distances $d_{\rm DM}$ inferred from the dispersion measures (DMs) were derived with the PyGEDM package¹⁴ (Price et al. 2021) based on two models of Galactic freeelectron distribution n_e : the NE2001 model (Cordes & Lazio 2002), and the YMW16 model (Yao et al. 2017). An indicative fractional uncertainty of 20% is prescribed to each DM-based distance.

5.1. Double Neutron Star Distances

Where parallax measurements are available, the parallaxbased distances are adopted as the DNS distances D (see Table 3). Otherwise, D is approximated by the weighted mean of the two DM-based distances $d_{\rm DM}$, where the uncertainty of D includes the indicative 20% fractional uncertainty and the standard deviation of the two d_{DM} . We note that the DM-based distances might be subject to additional systematic uncertainties (see Section 6); nevertheless, they will get increasingly reliable with time, as n_e models become better constrained with a growing number of independent pulsar distance measurements. The parallax-based distances of PSR J0509+3801 and PSR J1930-1852 were estimated in the same way as detailed in Section 6 of Ding et al. (2023b), while the parallax-based distances of the four other field DNSs with well-constrained parallaxes are directly quoted from respective publications (see Table 3 for the references).

5.2. Transverse Velocity Estimation and Caveats

Investigating the kinematics of Galactic DNSs ideally requires the knowledge of the 3D space velocity, $v^{\rm birth}$, of each DNS system immediately after its birth (which is inherently linked to the formation history and the SN properties

https://pypi.org/project/sterne/

¹² astrogeo.org/rfc/

https://www.atnf.csiro.au/research/pulsar/psrcat/

¹⁴ https://github.com/FRBs/pygedm

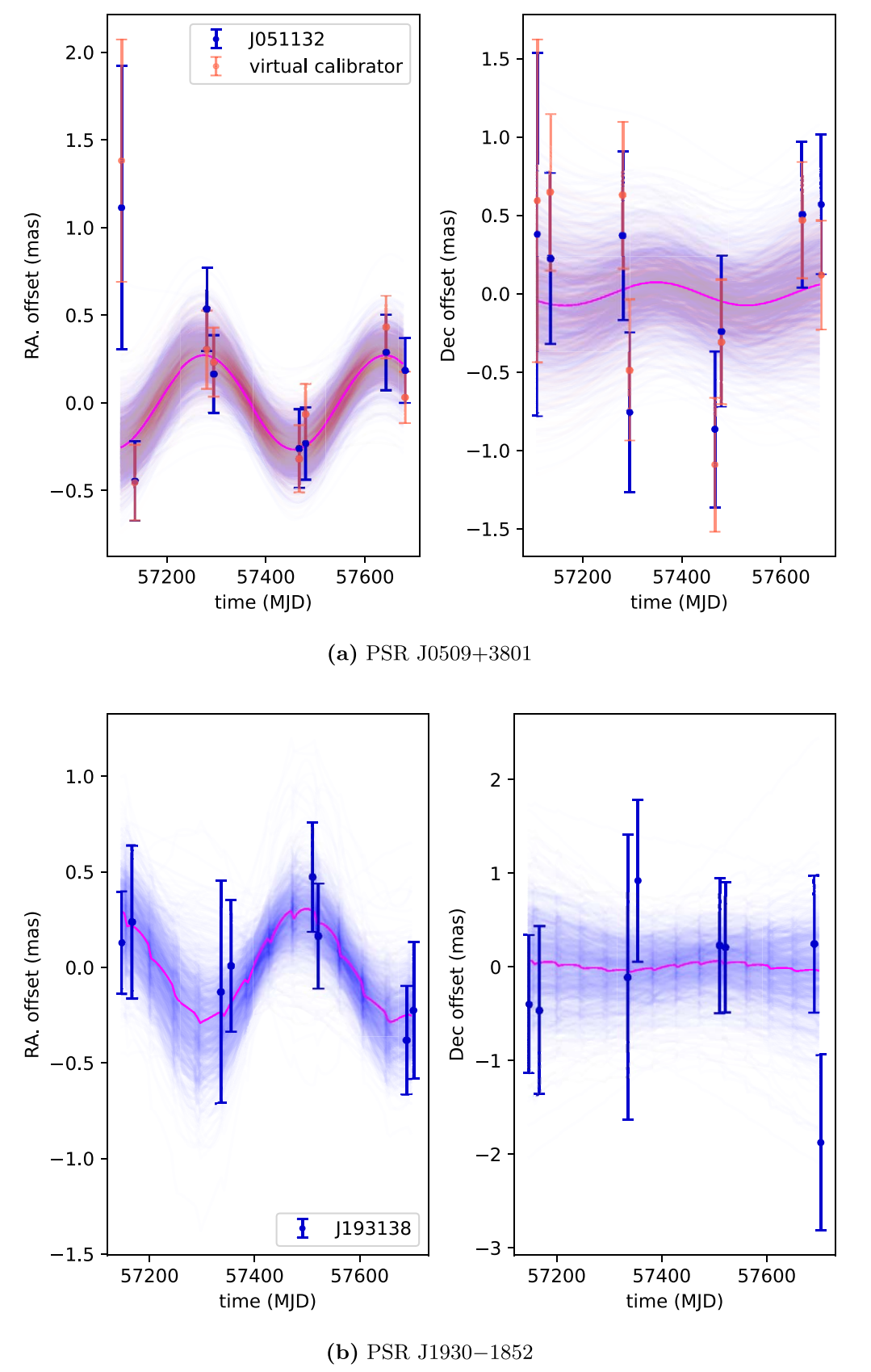


Figure 2. Sky position evolution with time after the removal of proper motion; parallax dominates, while orbital reflex motion is (almost) negligible. The best-fit astrometric model is outlined in pink, while Bayesian simulations are overlaid. The reference sources (see Table 1 for their full names) of the position measurements are provided in the legends. In particular, the astrometric model of PSR J0509+3801 is inferred from two series of positions measured with respect to two calibrators (see Section 3.1). Orbital parameters (i.e., orbital inclination and ascending node longitude) are only inferred (on top of other astrometric parameters) for PSR J1930 –1852, causing the small wobbles of the parallax signature in panel (b) (see Section 4 for more details).

 Table 2

 Inferred Astrometric Parameters and 68% Confidence Intervals for PSR J0509+3801 and PSR J1930-1852

Reference ^a Source	$\mu_{\alpha} \equiv \dot{\alpha} \cos \delta $ (mas yr ⁻¹)	μ_{δ} (mas yr ⁻¹)	ω (mas)	i _{orb} (deg)	$\Omega_{ m orb}$ (deg)	$\eta_{ ext{EFAC}}$
		PSR .	J0509+3801			
J051132	2.9(2)	-5.6(4)	0.30(10)			$1.1^{+0.7}_{-0.6}$
J050940	2.8(2)	-6.0(4)	0.25(12)			$2.7^{+1.4}_{-1.2}$
VC	2.8(2)	-6.1(5)	0.24(13)			$2.8^{+1.4}_{-1.0}$
VC+J051132	2.9(1)	-5.9(3)	0.27(7)			$1.4^{+0.6}_{-0.5}$
		PSR	J1930-1852			
J193138	4.3(2)	-5.2(4)	$0.29^{+0.12}_{-0.13}$	91+44	237^{+117}_{-114}	$0.6^{+0.5}_{-0.4}$

Notes

^a The in-beam calibrators listed in Table 1 are referred to with their right ascensions. "VC" stands for the virtual calibrator described in Figure 1 and Section 3.1.

^b The absolute reference positions of the DNSs are provided in Section 4.1.

of the system; e.g., Tauris et al. 2017). Here "space velocity" refers to the peculiar velocity with respect to the local stellar neighborhood of the DNS (see discussions in Section 6 of Ding et al. 2023b). In theory, $v^{\rm birth}$ of a DNS system can be derived from its current full kinematic information (including the 3D velocity and the 3D position) and the age, $t_{\rm age}$, of the secondborn NS, by applying a Galactic potential. This pathway to $v^{\rm birth}$ is, however, impractical, due to a highly uncertain value of $t_{\rm age}$ and the absence of the radial velocity, v_r , for all known Galactic DNSs. With measured proper motion and 3D position (from sky coordinates and distance) of a DNS, we can unfortunately only constrain its current transverse velocity, i.e., the 2D velocity along the plane of the sky, and thus only infer its 2D peculiar velocity, v_{\perp} , relative to the stellar neighborhood of the DNS system.

With no better option, this work uses v_{\perp} as a proxy of v_{\perp}^{birth} , i.e., the transverse velocity at birth, to probe the DNS kinematics. This approach hinges on the underlying assumption that v_{\perp} is largely correlated with v_{\perp}^{birth} , which is the first caveat to our analysis of DNS kinematics. Conceivably, this assumption holds more truth for DNSs with low space velocities, as their space velocities change less over time in the Galactic potential. Therefore, we expect that a v_{\perp} distribution compiled from a large number of DNSs should be close to the DNS $v_{\parallel}^{\text{birth}}$ distribution at the low space velocity end, while being more dispersed than the v_{\perp}^{birth} distribution at the high-space velocity end. Assuming that natal kicks are equally possible in all directions (isotropic kicks), it is easy to calculate that on average $v_{\perp}^{\text{birth}} = (\pi/4) \cdot v_{\perp}^{\text{birth}}$. Accordingly, we approximate the v_{\perp}^{birth} distribution by $(4/\pi) \cdot v_{\perp}$ in this work. To carefully justify the proposed v_{\perp} -to- $v_{\parallel}^{\text{birth}}$ mapping (as well as the coefficient $4/\pi$) requires much more data and a dedicated population analysis, which is, however, not possible

The v_{\perp} of the DNSs were calculated in a consistent manner following Section 6 of Ding et al. (2023b). The mathematical recipe of the calculation has been detailed in Verbunt et al. (2017). We evaluated the v_{\perp} uncertainties using Monte Carlo simulations, where proper motions and distances with asymmetric uncertainties were approached with split normal distributions (e.g., Possolo et al. 2019). In the v_{\perp} estimation, we approximated the motion of the stellar neighborhood of each DNS by a circular Galactocentric motion parallel to the Galactic plane. This treatment is conceivably less reliable for

DNSs \gtrsim 1 kpc away from the Galactic plane. Any anticorrelation (or correlation) between the Galactic height |z| and ν_\perp would suggest that the approximation is oversimplified and inappropriate. Though no correlation between |z| and ν_\perp is identified (see the top panel of Figure 3) with an insignificant Pearson correlation coefficient of $0.35^{+0.23}_{-0.24}$ (let alone a high false-alarm probability of 0.29; see Table 4), we cautiously note that additional systematics of ν_\perp are likely introduced by the approximation for the relatively high |z| DNSs. Due to the overly uncertain distance of PSR J1757–1854 (see Table 3, or Figure 13 of Cameron et al. 2023), we did not infer ν_\perp for PSR J1757–1854. Neither did we use it in the sample studies discussed in Section 7. The other 11 DNSs used in the sample studies are hereafter referred to as the 11 DNSs.

6. Individual DNS Systems

6.1. PSR J0509+3801

PSR J0509+3801 was discovered in the Green Bank Northern Celestial Cap Pulsar Survey at 350 MHz (Stovall et al. 2014) and later identified as a DNS system in a highly eccentric (e = 0.586) 9.1 hr orbit (Lynch et al. 2018). The pulsar mass and the companion mass of the system are well determined thanks to the significant measurements of the periastron advance and the gravitational redshift (Lynch et al. 2018). Among the 12 field DNSs having proper-motion measurements, PSR J0509+3801 possesses the second-highest orbital eccentricity. Therefore, the relatively precise determination of v_{\perp} for PSR J0509+3801 (see Table 2) is crucial for probing the v_{\perp} -to-e correlation (see Section 7.1). By comparing the parallax-based distance of PSR J0509+3801 to the two DM distances, we find that, at $\approx 2\sigma$ confidence, both DM distances (based on the NE2001 and the YMW16 n_e models) are underestimated.

6.2. PSR J1930-1852

PSR J1930–1852 is the sixth pulsar discovered by students attending the Pulsar Search Collaboratory (Rosen et al. 2013) from the drift-scan observations made with the GBT at 350 MHz (Boyles et al. 2013; Lynch et al. 2013). PSR J1930 –1852 is an exceptional DNS system: it challenges the DNS formation theory with the longest P_s (185.5 ms) and the widest ($P_b = 45$ days) orbit among the Galactic field DNSs (Swiggum et al. 2015; see also Table 3). Accordingly, the astrometric

Table 3

Distances and Space Velocities of Astrometrically Measured Field Double Neutron Stars

Distinces and opace resolutes of risubmedically reasoned read basis								
PSR	l (deg)	b (deg)	P _s (ms)	P _b (days)	e	${m_{ m p}}^{ m a} \ (M_{\odot})$		$m_{ m c}^{ m a} (M_{\odot})$
J0509+3801 (9)	168.3	-1.2	76.5	0.38	0.59	1.36(8)		1.45(8)
J0737-3039A B(1)	245.2	-4.5	22.7 2773	0.10	0.088	1.33819(1))	1.24887(1)
J1518+4904 (2)	80.8	54.3	40.9	8.6	0.25	$1.470^{+0.030}_{-0.034}$)	$1.248^{+0.035}_{-0.029}$
B1534+12 (10)	19.8	48.3	37.9	0.42	0.27	1.3330(2)		1.3455(2)
B1913+16 (3)	50.0	2.1	59.0	0.32	0.62	1.438(1)		1.390(1)
J1930-1852 (11)	20.0	-16.9	185.5	45.1	0.40	<1.32		>1.30
J0453+1559 (4)	184.1	-17.1	45.8	4.1	0.11	1.559(5)		1.174(4)
J1411+2551 (5)	33.4	72.1	62.5	2.62	0.17	< 1.62		>0.92
J1756-2251 (6)	6.5	0.95	28.5	0.32	0.18	1.341(7)		1.230(7)
J1757-1854 (12)	10.0	2.9	21.5	0.18	0.61	1.3412(4)		1.3917(4)
J1829+2456 (7)	53.3	15.6	41.0	1.18	0.14	1.306(4)		1.299(4)
J1913+1102 (8)	45.3	0.19	27.3	0.21	0.090	1.62(3)		1.27(3)
PSR	μ_{lpha} (mas yr $^{-1}$)	μ_{δ}	$d_{\rm DM}^{\rm (NE)\ b}$	$d_{\rm DM}^{\rm (YMW)}$ b		D°	(km s^{-1})	
	(mas yr)	(mas yr ⁻¹)	(kpc)	(kpc)		(kpc)	, ,	
J0509+3801 (9)	2.9(1)	-5.9(3)	1.9(4)	1.6(3)		$4.2^{+1.6}_{-0.9}$	118_{-30}^{+47}	
J0737-3039A B (1)	-2.57(3)	2.08(4)	0.5(1)	1.1(2)		0.74(6)	5.9(5)	
J1518+4904 (2)	-0.68(3)	-8.53(4)	0.6(1)	1.0(2)		0.81(2)	16.0(6)	
B1534+12 (10)	1.484(7)	-25.29(1)	0.9(2)	0.9(2)		$0.94^{+0.07}_{-0.06}$	102^{+8}_{-7}	
B1913+16 (3)	$-0.77^{+0.16}_{-0.06}$	$0.01^{+0.10}_{-0.17}$	6(1)	5(1)		$4.1^{+2.0}_{-0.7}$	141^{+59}_{-43}	
J1930-1852	4.3(2)	-5.2(4)	1.5(3)	2.0(4)		$4.6^{+2.4}_{-1.4}$	152^{+91}_{-49}	
J0453+1559 (4)	-5.5(5)	-6.0(4.2)	1.1(2)	0.5(1)		0.6(4)	26^{+16}_{-12}	
J1411+2551 (5)	-3(12)	-4(9)	1.0(2)	1.1(2)		1.1(2)	63^{+47}_{-32}	
J1756-2251 (6)	-2.42(8)	0(2)	2.5(5)	2.8(6)		2.6(6)	30^{+16}_{-9}	
J1757-1854 (12), ^d	-4.48(11)	-0.5(12)	7.4(1.5)	19.5(3.9)		9(7)		
J1829+2456 (7)	-5.51(6)	-7.8(1)	1.2(2)	0.9(2)		1.1(3)	24^{+7}_{-8}	
J1913+1102 (8)	-3.0(5)	-8.7(1.0)	7.6(1.5)	7.1(1.4)		7.3(1.5)	94^{+40}_{-33}	
• *	* *	` ′	` '	` /		* *	23	

Notes

References. (1) Kramer et al. (2021a), (2) Tan et al. (2024), Ding et al. (2023b), (3) Weisberg & Huang (2016), Deller et al. (2018), (4) Martinez et al. (2015), (5) Martinez et al. (2017), (6) Ferdman et al. (2014), (7) Haniewicz et al. (2021), (8) Ferdman et al. (2020), (9) Lynch et al. (2018), (10) Fonseca et al. (2014), Ding et al. (2023b), (11) Swiggum et al. (2015), (12) Cameron et al. (2023).

determination of PSR J1930–1852 is important for investigating the v_{\perp} -to- P_s and v_{\perp} -to- P_b correlations (see Section 7.1). Unfortunately, we did not achieve significant parallax measurement for PSR J1930–1852, due to its radio weakness: random errors dominate the error budget of the position series. In this regard, the parallax precision of PSR J1930–1852 can be potentially enhanced by a factor of \gtrsim 4 in the future with high-sensitivity VLBI arrays like the High Sensitivity Array.

7. Sample Studies of DNS Kinematics

7.1. Broad Correlation Analysis

The 3D systemic space velocity, v^{birth} , at DNS birth, right after the second SN, is acquired from the combination of the

anisotropic nature (i.e., natal momentum kick) and instantaneous mass loss of the SN producing the second-born NS. Therefore, it has been proposed that v^{birth} is likely correlated with a few parameters that include the orbital eccentricity, e, the orbital period, P_b , and the companion mass m_c (e.g., Tauris et al. 2017; Haniewicz et al. 2021). Despite the caveats of v_{\perp} estimation (see Section 5.2), we investigate whether v_{\perp} is correlated with the aforementioned parameters. In addition to v_{\perp} , another important indicator of DNS kinematics is the DNS distance |z| from the Galactic plane, which has also been refined with VLBI astrometry of DNSs. Assuming that DNS systems were born in the Galactic plane and received natal kicks in random directions, DNSs with large space velocities are more likely found at high |z|. To comprehensively examine

^a The m_p and m_c stand for, respectively, the first-born NS mass and the second-born NS mass. The mass uncertainties quoted for PSR J1829+2456 components are half the 95.4%-confidence-level uncertainties reported by Haniewicz et al. (2021).

b $d_{
m DM}^{
m (NE)}$ and $d_{
m DM}^{
m (NE)}$ represent the DM-based distances based on the NE2001 Galactic free-electron distribution model (Cordes & Lazio 2002) and the YMW16 model (Yao et al. 2017), respectively. All DM-based distances were acquired with the PyGEDMpackage (see footnote 14). Indicative 20% fractional uncertainties are applied to both $d_{
m DM}^{
m (NE)}$ and $d_{
m DM}^{
m (NE)}$.

^c For the upper block, where the parallaxes have been constrained, parallax-based distances are reported and used for the calculation of the space velocities v_{\perp} . In particular, the distances of PSR J0509+3801 and PSR J1930-1852 were estimated in the same way as in Ding et al. (2023b) (see Section 5). For any pulsar in the lower block where no parallax constraint is available yet, the distance is approximated by the weighted average of the two DM-based distances; the distance uncertainty consists of (1) the weighted standard deviation of the two DM-based errors and (2) the 20% fractional uncertainty on the larger one of the two DM-based distances.

^d PSR J1757-1854 is not included in the sample studies of this paper due to the highly uncertain distance.

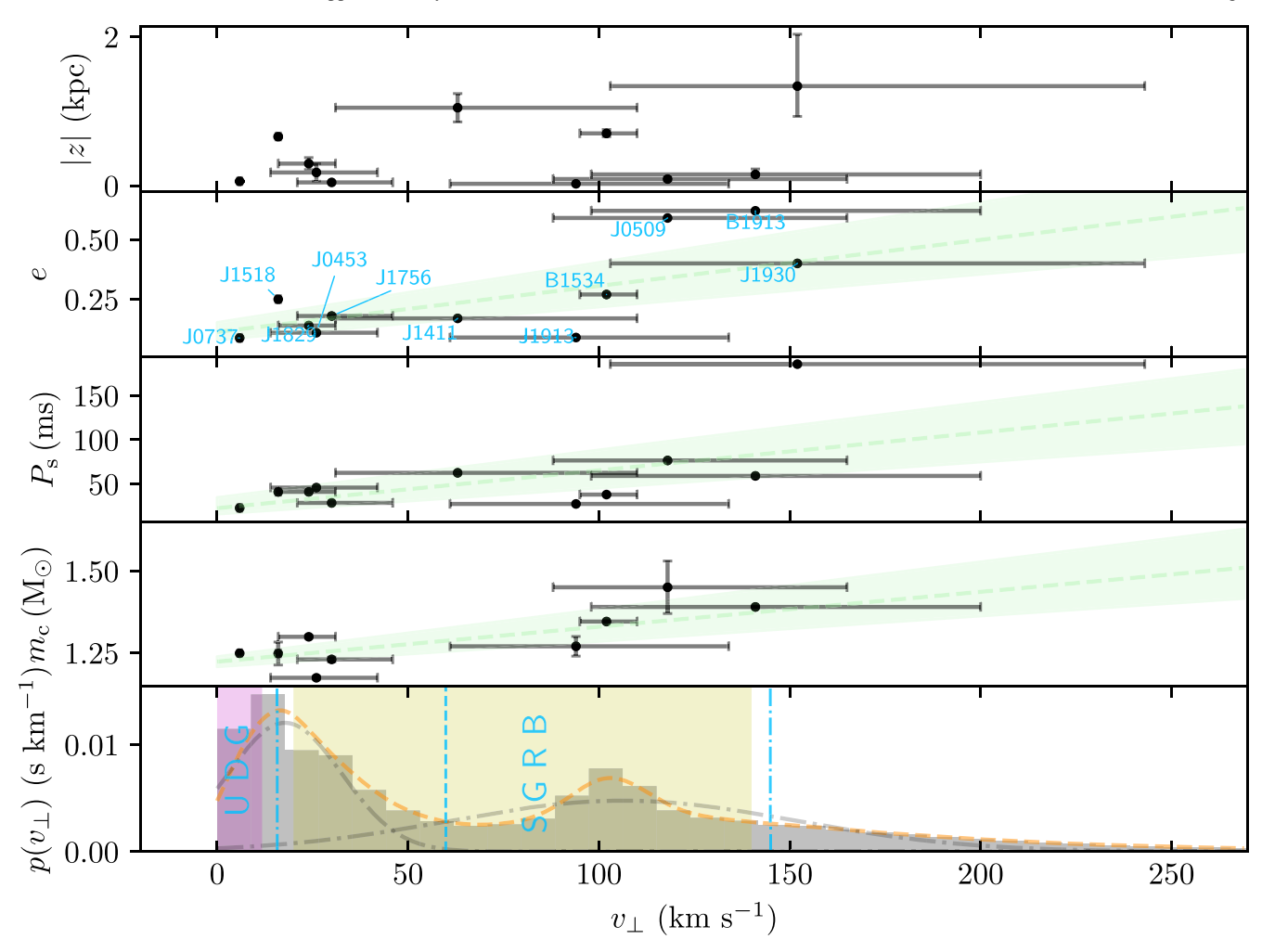


Figure 3. Top: DNS transverse peculiar velocities, v_{\perp} , vs. vertical distances, |z|, from the Galactic plane, from which no correlation is identified between v_{\perp} and |z|. Upper middle: v_{\perp} vs. orbital eccentricity, e, where each DNS is marked with its R.A. The best linear fit is given by $e = 1.9^{+0.6}_{-0.6} \times 10^{-3} \cdot v_{\perp} + 0.11^{+0.04}_{-0.03}$ (green dashed line, while the green shade reflects the uncertainties). Middle: v_{\perp} vs. spin period, P_s , of the first-born NS. The best linear fit is given by $P_s = 0.43^{+0.11}_{-0.13}$ ms. $v_{\perp} + 23^{+12}_{-1}$ ms. Lower middle: v_{\perp} vs. companion mass m_c . The best linear fit is given by $m_c = 1.1^{+0.4}_{-0.3} \times 10^{-3} M_{\odot} \cdot v_{\perp} + 1.222^{+0.016}_{-0.016} M_{\odot}$. In all the linear fitting relations of the three panels in the middle, v_{\perp} is stated in km s⁻¹. Bottom: the pdf of v_{\perp} approached by Monte Carlo resampling (see Section 7.2.). The vertical lines present the 16th, 50th, and 84th percentiles of the cumulative distribution function of v_{\perp} . Overlaid are the shaded v_{\perp} ranges required for consistency with the observations of UFDGs ($<\pi/4 \cdot 15$ km s⁻¹; see Section 7.2.2) and extragalactic SGRBs (20–140 km s⁻¹; see Section 7.2.1). The dashed curve in dark orange shows the v_{\perp} pdf smoothed with kernel density estimation (using scipy.stats.Gaussian_kde, where the bandwidth is determined automatically), while the two dashed—dotted curves (in black) present the two Gaussian components fitted toward the smoothed v_{\perp} pdf (see Section 7.2 for details). The two Gaussian components are plotted for the sole purpose of demonstration, as the unimodality of the current v_{\perp} pdf cannot be ruled out owing to the small sample size of v_{\perp} (see Section 7.2.3).

the correlation between the two DNS kinematics indicators (i.e., v_{\perp} and |z|) and other parameters, we carried out linear and power-law correlation analyses on seven parameters: v_{\perp} , |z|, e, P_b , spin period (of the first-born and recycled NS) P_s , m_c , and pulsar mass m_p . The calculated Pearson correlation coefficients ρ and their false-alarm probabilities (or p-values) P_F are summarized in Table 4, where the two DNS systems (i.e., PSR J1930–1852 and PSR J1411+2551) that have not had significant measurements of the pulsar mass are excluded from the calculation of mass-related Pearson correlation coefficients.

A correlation is normally considered tentative when $0.5 \lesssim |\rho| \lesssim 0.75$ and $P_F < 0.05$, while being strong if $\rho \gtrsim 0.75$ and $P_F < 0.05$. Unsurprisingly, two of the examined parameters (i.e., P_s and |z|) are well correlated with P_b . These correlations are thought to have an origin in binary stellar evolution. For example, Tauris et al. (2015, 2017) demonstrated that the wider the pre-SN binary's orbit is, the less efficient the final case BB mass transfer to the first-born NS is (the reason being a shorter

lifetime prior to the core collapse of more evolved helium star donors, i.e., the progenitors of the second-born NSs). Therefore, after the second SN, wider-orbit DNS systems have, on average, slower-spinning recycled NSs compared to more tightorbit DNS systems. This is confirmed from our analysis, which yields a Pearson correlation coefficient of $\rho = 0.92$. Due to the unique kick magnitude and direction of each DNS system, some scatter is expected in the final correlation between P_b and P_s . Tauris et al. (2015, 2017) also argued for weak correlations between e and both P_b and P_s . We find that the inclusion of PSR J1930–1852, which has exceptionally long P_b and P_s (Swiggum et al. 2015) among Galactic field DNSs, plays an essential role in dismissing the e-to- P_b correlation. But even without PSR J1930–1852, a tentative e-to- P_b correlation is not revealed by our small sample. On the other hand, a tentative logarithmic correlation between e and P_s is identified, even when PSR J1930–1852 with the long P_s of 185.5 ms is included.

Table 4
Pearson Coefficients for (upper) Linear Correlation and (lower) Logarithmic-scale Correlation, and Their False-alarm Probabilities

	e	P_s	P_b	m_p	m_c	z
$\overline{v_{\perp}}$	0.68 ^{+0.12} _{-0.15} 0.022	0.65 ^{+0.17} _{-0.24} 0.029	$0.45^{+0.23}_{-0.28} \ 0.16$	$0.12^{+0.18}_{-0.20}$ 0.76	0.74 ^{+0.10} _{-0.15} 0.024	$0.35^{+0.23}_{-0.24}$ 0.29
z	$0.12^{+0.05}_{-0.07}$ 0.72	0.75 ^{+0.10} _{-0.18} 0.008	0.78 ^{+0.11} _{-0.19} 0.005	$-0.16^{+0.11}_{-0.11} 0.68$	$0.05^{+0.16}_{-0.12}$ 0.89	
m_c	0.83 ^{+0.03} _{-0.06} 0.006	$0.72^{+0.07}_{-0.14}$ 0.03	$-0.40^{+0.12}_{-0.11} 0.29$	$-0.34^{+0.16}_{-0.14} 0.37$		
m_p	$-0.19^{+0.14}_{-0.12} 0.62$	$-0.07^{+0.18}_{-0.17} 0.85$	$0.32^{+0.09}_{-0.10}$ 0.40			
P_b	0.20 0.55	0.92 0.00006				
P_s	0.47 0.14					
			(upper)			
	lg <i>e</i>	$\lg P_s$	$\lg P_b$	$\lg m_p$	$\lg m_c$	$\lg z $
$\overline{\lg v_{\perp}}$	0.63 ^{+0.07} _{-0.08} 0.040	0.61 ^{+0.08} _{-0.10} 0.047	$0.15^{+0.09}_{-0.11}$ 0.65	$0.18^{+0.15}_{-0.17}$ 0.64	$0.63^{+0.10}_{-0.11}$ 0.07	$0.22^{+0.11}_{-0.12}$ 0.51
$\lg z $	0.38(6) 0.25	0.64 ^{+0.04} _{-0.06} 0.036	0.75 ^{+0.04} _{-0.07} 0.008	$-0.24^{+0.12}_{-0.13} 0.53$	$0.15^{+0.18}_{-0.15} \ 0.70$	
$\lg m_c$	0.78 $^{+0.05}_{-0.07}$ 0.013	$0.63^{+0.06}_{-0.11}$ 0.07	$-0.35^{+0.10}_{-0.09} 0.35$	$-0.34^{+0.17}_{-0.15} 0.37$		
$\lg m_p$	$-0.26^{+0.13}_{-0.12} 0.50$	$-0.02^{+0.17}_{-0.16} 0.95$	$0.28^{+0.07}_{-0.08}$ 0.47			
$\lg P_b$	0.21 0.54	0.71 0.014				
$\lg P_s$	0.67 0.024					
			(lower)			

Note. The numbers on the left and right side of "|" are the Pearson correlations coefficients ρ and the associated p-values P_F , respectively. The uncertainties of the correlation coefficients reflect the errors of m_p , m_c , and v_{\perp} and were estimated using Monte Carlo simulations. The p-values, or the false-alarm probabilities of the correlation strengths, are calculated with the median ρ of the simulations. $|\rho| > 0.5$ with $P_F < 0.05$ are considered to suggest correlations and are highlighted in bold.

Between the two kinematics indicators, v_{\perp} and |z|, we did not find any significant correlation, which is the precondition of the v_{\perp} estimation (see Section 5.2). However, v_{\perp} and |z|apparently show correlations with the other parameters: v_{\perp} is tentatively correlated with e and m_c (see Figure 3), while |z| is well correlated with P_b . In addition, both kinematics indicators are correlated with P_s (see Figure 3). Large SN kicks will, in general, result in relatively large eccentricities. Hence, the former correlation between v_{\perp} and e is perhaps not surprising. There are several components that affect the SN outcome: large kicks will disrupt the binaries. Because of the strong dependence on the stochastic kick direction in the second SN, as well as the different masses of the naked helium stars resulting from the previous common-envelope phase, it is nontrivial to directly link kinematic parameters $(v_{\perp} \text{ and } |z|)$ of DNS systems to their orbital parameters and component masses. A proposed correlation between the SN kick velocity magnitude and the resulting NS mass (Tauris et al. 2017) would translate into a (weaker) correlation between, e.g., v_{\perp} or |z| and m_c . Our analysis confirms the postulated correlation between v_{\perp} and m_c , while finding no correlation between |z| and m_c . On the other hand, any correlation between |z| (or v_{\perp}) and P_s is somewhat unexpected and nontrivial to explain.

We note that great caution must be taken with postulating correlations involving parameters that evolve with time, such as P_s and e. To properly analyze the DNS population, time evolution must be included (e.g., Tauris et al. 2017). Future analysis with more DNS systems will likely improve the statistical significance of the tentative correlations suggested in this work. Given no indication of insufficient e or P_s coverage in the pulsar search programs (which led to the discoveries of the Galactic DNSs), no selection bias is uncovered for the v_{\perp} distribution. Among the four abovementioned correlations between the two kinematics indicators and other parameters, linear correlations are either preferred over or comparable to the power-law counterparts by ρ and P_F (see Table 4). This

conclusion can also be drawn for the whole Table 4, with the $\{e, P_s\}$ pair being the only exception.

7.2. The Transverse Peculiar Velocity Distribution of Field Double Neutron Stars and Its Implications

As noted in Section 5.2, a v_{\perp} distribution based on a large sample of astrometrically measured DNSs is expected to better approximate the v_{\perp}^{birth} distribution at the low-velocity end, while being more dispersed than the v_1^{birth} counterpart at the high-velocity end. With this in mind, we compiled the v_{\perp} results in Table 3 to a DNS v_{\perp} distribution using Monte Carlo resampling. Specifically, we assume that all of the 11 field DNSs equally represent the whole population of field DNSs, and we randomly drew 10,000 values of v_{\perp} for each DNS from a split normal distribution. Subsequently, the $11 \times 10,000$ randomly drawn values of the DNSs were concatenated together. From this resampled v_{\perp} chain, we estimated v_{\perp} of field DNSs to be 60^{+85}_{-44} km s⁻¹ (see Figure 3); hence, the 3D space velocities of field DNSs should be $\sim 4/\pi \times 60 \text{ km s}^{-1} = 76 \text{ km s}^{-1}$ (see Section 5.2). Here the median of the v_{\perp} chain is adopted as the v_{\perp} estimate, while the central 68% of the v_{\perp} chain is used as the v_{\perp} uncertainty interval. To mitigate binning effects, we smoothed the histogram of the ν_{\perp} simulations with kernel density estimation provided by scipy.stats.Gaussian_kde. The resultant dashed curve (in the bottom panel of Figure 3) represents the estimated probability density of distribution (pdf) of v_{\perp} .

7.2.1. Consistency with Extragalactic Short γ -Ray Burst Localizations

As mentioned in Section 1.2, transverse velocities $v_{\perp}^{\rm SGRB}$ of SGRBs have been evaluated to be \approx 20–140 km s⁻¹ using projected SGRB displacements from the expected birth sites in their host galaxies, assuming that the SGRBs are associated with NS–NS mergers (Fong & Berger 2013). It is timely to note that the $v_{\perp}^{\rm SGRB}$ estimation also has its caveats, hence being subject to additional systematic errors. For example, the

estimation hinges on the reliability of the DNS delay time distribution. Besides, the distances to the SGRB host galaxies (and hence their projected sizes) are estimated with cosmological redshifts assuming negligible peculiar velocities. Nevertheless, the ν_{\perp}^{SGRB} inferred by Fong & Berger (2013) is highly consistent with our estimate of $\nu_{\perp}=60^{+85}_{-44}~\rm km~s^{-1}$ (see also the bottom panel of Figure 3), which supports the idea that the observed extragalactic SGRBs are indeed driven by NS–NS mergers and suggests that the underlying DNS delay time provided by Leibler & Berger (2010) is reasonable. The consistency between ν_{\perp}^{SGRB} and ν_{\perp} strengthens the new research opportunity to be proposed in Section 8.2.

7.2.2. Implications on the r-process Element Production in Ultrafaint Dwarf Galaxies

UFDGs are old and metal-poor satellite galaxies dominated by dark matter (Simon & Geha 2007). However, a small fraction of UFDGs are found to have exceptionally high abundance of r-process elements (Ji et al. 2016; Hansen et al. 2017, 2020), which is still poorly understood. If DNS mergers contributed to the r-process enrichment in UFDGs, the DNSs would either be gravitationally bound to the UFDG or be able to merge within \sim 1 Myr (so that the produced r-process elements can potentially be recycled in the UFDG; Safarzadeh et al. 2019). As the latter possibility is disfavored by recent DNS delay time studies that show that most DNSs need \gtrsim 10 Myr to merge (Andrews & Zezas 2019; Zevin et al. 2022), examining the former possibility with the DNS space velocity distribution becomes crucial for understanding the origin of the r-process enrichment in UFDGs.

To be gravitationally bound to a UFDG, DNSs are expected to have $v_{\perp} < \pi/4 \cdot v_{\rm esc}^{\rm UFDG}$ on average, where the UFDG escape velocity $v_{\rm esc}^{\rm UFDG}$ is typically only 15 km s⁻¹ (Beniamini et al. 2016) and is limited to \lesssim 25 km s⁻¹ (Safarzadeh et al. 2019). According to the current v_{\perp} distribution, the probability that $v_{\perp} < \pi/4 \cdot v_{\rm esc}^{\rm UFDG}$ is 11% and 25%, respectively, for $v_{\rm esc}^{\rm UFDG} = 15$ km s⁻¹ and $v_{\rm esc}^{\rm UFDG} = 25$ km s⁻¹. In other words, \sim 11% of the DNSs born in UFDGs are expected to be gravitationally bound to the LIEDGs. Here we assume that the gravitationally bound to the UFDGs. Here we assume that the Galactic DNS v_{\perp} distribution can well approximate the UFDG counterpart. This assumption might not be true, due to the different properties of UFDGs and the Galaxy. In particular, the generally much lower metallicities in UFDGs (Fu et al. 2023) would reduce the minimum initial mass of progenitor stars required for CCSNe (Han et al. 1994) and shift downward the mass range of progenitor stars that lead to ECSNe (Podsiadlowski et al. 2004). Accordingly, it is likely that the DNS v_{\perp} distribution in UFDGs is systematically lower than the Galactic counterpart. In this regard, $\sim 11\%$ might only be a lower limit to the fraction of DNSs gravitationally bound to the UFDGs. The relation between the DNS space velocity distribution and the average metallicity of the host galaxy has not been well characterized and is highly desired by our investigation (of the origin of the r-process elements in UFDGs using the kinematics of Galactic DNSs). Due to the small sample size of v_{\perp} , the estimated fraction of DNSs bound to UFDGs is still indicative. Nevertheless, the estimation will become increasingly accurate when more astrometrically determined DNSs are available.

On the other hand, being bound to a UFDG does not guarantee *r*-process enrichment through DNS mergers: the DNSs are additionally required to merge within 1 Gyr, so that the mergers precede the cessation of the star formation in

UFDGs (Brown et al. 2014; Weisz et al. 2014). In addition, DNSs receiving the smallest kicks usually have smaller eccentricities, which tend to increase the merger timescales. Therefore, we expect a lower but still significant fraction of gravitationally bound DNSs eventually contributing to the r-process enrichment in UFDGs, given that the $\lesssim 1$ Gyr merger time requirement is not hard to meet (Zevin et al. 2022).

7.2.3. A Road Map for Testing Multimodality of the v_{\perp} Distribution

It has been proposed that a ν_{\perp} distribution of an NS subgroup (e.g., millisecond pulsars or magnetars) can be used to probe the formation mechanism of that subgroup (e.g., Tauris & Bailes 1996; Ding 2022; Ding et al. 2023a, 2023b). The same scientific goal can be pursued with a DNS ν_{\perp} distribution. Although the ν_{\perp} distribution we compile is based on only 11 isolated DNS systems, some global properties of the distribution may have emerged. In particular, an apparent bimodal feature can be seen in the estimated ν_{\perp} pdf (see the bottom panel of Figure 3).

To test the multimodality (including bimodality) of the sample of the 11 ν_{\perp} measurements, we employed Hartigan's dip test (Hartigan 1985; Hartigan & Hartigan 1985), which starts from the null hypothesis that the v_{\perp} distribution is unimodal and then examines the likelihood P_{Null} (also known as p-value) of the null hypothesis being true. In order to accommodate v_{\perp} uncertainties, we carried out the dip test by the following procedure. We first resampled 10,000 sets of 11 v_{\perp} (one v_{\perp} per DNS per set), assuming split normal distribution for v_{\perp} of each DNS. From every set, one p-value was acquired using the diptest 15 Python package (also see https://cran.rproject.org/web/packages/diptest/index.html for the earlier R package). Finally, the mean of the 10,000 p-values is adopted as the P_{Null} estimate. In this way, we obtained $P_{\text{Null}} = 50\%$, which suggests that no conclusion can be drawn with regard to the multimodality of the current v_{\perp} distribution.

The large P_{Null} is not surprising given the small sample size (of 11). If the observed v_{\perp} pdf (in Figure 3) and the bimodality are true, we find that about 120 and 160 additional astrometrically determined DNSs are required to rule out unimodality of the v_{\perp} sample at 90% and 95% confidence, respectively. This prospect (of probing multimodality of the v_{\perp} distribution) might be realized in the next decade with the ongoing and future pulsar search programs utilizing highsensitivity pulsar timing facilities such as FAST (e.g., Li & Pan 2016; Han et al. 2021; Miao et al. 2023), MeerKAT (e.g., Bailes et al. 2020; Kramer et al. 2021b), ngVLA (e.g., Murphy et al. 2018; McKinnon et al. 2019), and the Square Kilometre Array (e.g., Dewdney et al. 2009; Keane et al. 2015). If unimodality of the v_{\perp} distribution can be ruled out at high confidence, one can proceed to decompose the v_{\perp} pdf into multiple modes and investigate the likely formation channel(s) associated with each mode. For example, if in the future ~ 160 isolated DNSs were found to follow a bimodal v_{\perp} distribution similar to the one in Figure 3, a bimodal Gaussian distribution could be fitted against the future v_{\perp} pdf. For the only purpose of demonstration, the best-fit Gaussian components for the current v_{\perp} pdf (estimated in this work) are illustrated with the two dashed-dotted curves in the bottom panel of Figure 3.

¹⁵ https://github.com/RUrlus/diptest

8. Conclusions and Future Prospects

8.1. Conclusions

In this work, we measured proper motions and parallaxes for two DNS systems, PSR J0509+3801 and PSR J1930-1852, with VLBA observations. In a consistent manner, we estimated the two kinematic indicators, the transverse space velocity v_{\perp} and the vertical height |z|, for all Galactic DNSs astrometrically measured (see Section 5). With this small sample of 11, we investigated the correlation between the kinematic indicators and five other parameters: the orbital period P_b , the spin period P_s , the orbital eccentricity e, the companion mass m_c , and the pulsar mass m_p . Tentative correlations were identified between v_{\perp} and e, v_{\perp} and P_s , v_{\perp} and m_c , |z| and P_s , and |z| and P_b (see Section 7.1). By combining the v_{\perp} estimates, we obtained the preliminary v_{\perp} distribution of DNSs (see Section 7.2), which is used to pursue three scientific studies. First, we found that the v_{\perp} distribution is consistent with the indicative transverse velocities v_{\perp}^{SGRB} of SGRBs evaluated by Fong & Berger (2013), which suggests that the underlying DNS delay time provided by Leibler & Berger (2010) is reasonable. Second, according to the v_{\perp} distribution and the typical escape velocity of UFDGs, ≥11% of the DNSs born in UFDGs are gravitationally bound to UFDGs. We argue that a significant fraction of the DNSs gravitationally bound to UFDGs would eventually contribute to the r-process enrichment of the UFDGs. Therefore, DNS mergers cannot be ruled out as the source of r-process enrichment in UFDGs. Finally, we looked into the prospects of using the v_{\perp} distribution to probe the formation channels of DNSs. Our simulation suggests that astrometric measurements of ~120 additional isolated DNSs were needed to rule out unimodality of the v_{\perp} distribution at 90% confidence, if the v_{\perp} distribution shown in Figure 3 is true.

8.2. Future Prospects

- 1. The availability of the three components—the v_⊥ distribution (directly approached with Galactic DNSs), the SGRB displacements from the expected birth sites in the host galaxies (e.g., Fong et al. 2022; O'Connor et al. 2022), and the DNS delay time distribution (constrained by Galactic DNSs, SGRB host galaxies, and GW events; e.g., Andrews & Zezas 2019; Beniamini & Piran 2019; Zevin et al. 2022)—promises a new research opportunity: by combining the knowledge of the three components, one can uncover the selection biases (in the three components) to unprecedented details and achieve the most reliable posterior distributions for the three components.
- 2. As mentioned in Section 7.2.3, ongoing and future relativistic binary pulsar search programs using high-sensitivity radio telescopes (or tied arrays) will drastically increase the number of Galactic DNSs, which will eventually enable the multimodality test of the v_{\perp} distribution and refine the estimation of the fraction of DNSs gravitationally bound to UFDGs (see Section 7.2.2). Meanwhile, high-sensitivity VLBI observations of DNSs will not only increase the number of DNSs well measured astrometrically but also achieve higher astrometric precision for the DNSs.

Acknowledgments

H.D. acknowledges the EACOA Fellowship awarded by the East Asia Core Observatories Association. J.K.S., R.S.L., and S.C. are members of the NANOGrav Physics Frontiers Center, which is supported by NSF award PHY-1430284. This work is based on observations with the Very Long Baseline Array (VLBA), which is operated by the National Radio Astronomy Observatory (NRAO). The NRAO is a facility of the National Science Foundation operated under cooperative agreement by Associated Universities, Inc. This work made use of the Swinburne University of Technology software correlator, developed as part of the Australian Major National Research Facilities Programme and operated under license (Deller et al. 2011).

Software: numpy (Harris et al. 2020), scipy (Virtanen et al. 2020), astropy (Astropy Collaboration et al. 2013, 2018, 2022), matplotlib (Hunter 2007), bilby (Ashton et al. 2019), psrqpy (Pitkin 2018), adjustText¹⁶ (Flyamer et al. 2024).

ORCID iDs

```
Hao Ding https://orcid.org/0000-0002-9174-638X
Adam T. Deller https://orcid.org/0000-0001-9434-3837
Joseph K. Swiggum https://orcid.org/0000-0002-1075-3837
```

Ryan S. Lynch https://orcid.org/0000-0001-5229-7430 Shami Chatterjee https://orcid.org/0000-0002-2878-1502 Thomas M. Tauris https://orcid.org/0000-0002-3865-7265

References

Abbott, B. P., Abbott, R., Abbott, T., et al. 2017a, PhRvL, 119, 161101

```
Abbott, B. P., Bloemen, S., Canizares, P., et al. 2017b, ApJL, 848, L12
Andrews, J. J., & Zezas, A. 2019, MNRAS, 486, 3213
Annala, E., Gorda, T., Kurkela, A., & Vuorinen, A. 2018, PhRvL, 120, 172703
Ashton, G., Hübner, M., Lasky, P. D., et al. 2019, ApJS, 241, 27
Astropy Collaboration, Price-Whelan, A. M., Lim, P. L., et al. 2022, ApJ,
Astropy Collaboration, Price-Whelan, A. M., Sipőcz, B. M., et al. 2018, AJ,
  156, 123
Astropy Collaboration, Robitaille, T. P., Tollerud, E. J., et al. 2013, A&A,
Bailes, M., Jameson, A., Abbate, F., et al. 2020, PASA, 37, e028
Beniamini, P., Hotokezaka, K., & Piran, T. 2016, ApJL, 829, L13
Beniamini, P., & Piran, T. 2016, MNRAS, 456, 4089
Beniamini, P., & Piran, T. 2019, MNRAS, 487, 4847
Bloom, J. S., Sigurdsson, S., & Pols, O. R. 1999, MNRAS, 305, 763
Boyles, J., Lynch, R. S., Ransom, S. M., et al. 2013, ApJ, 763, 80
Brown, T. M., Tumlinson, J., Geha, M., et al. 2014, ApJ, 796, 91
Burrows, A., Wang, T., Vartanyan, D., & Coleman, M. S. B. 2023, arXiv:2311.
Cameron, A., Bailes, M., Champion, D., et al. 2023, MNRAS, 523, 5064
Cameron, A., Champion, D., Kramer, M., et al. 2018, MNRAS Letters,
Cordes, J. M., & Lazio, T. J. W. 2002, arXiv:astro-ph/0207156
Coward, D., Howell, E., Piran, T., et al. 2012, MNRAS, 425, 2668
Deller, A., Boyles, J., Lorimer, D., et al. 2013, ApJ, 770, 145
Deller, A. T., Brisken, W. F., Phillips, C. J., et al. 2011, PASP, 123, 275
Deller, A. T., Goss, W. M., Brisken, W. F., et al. 2019, ApJ, 875, 100
Deller, A. T., Vigeland, S. J., Kaplan, D. L., et al. 2016, ApJ, 828, 8
```

Deller, A. T., Weisberg, J. M., Nice, D. J., & Chatterjee, S. 2018, ApJ,

Dewdney, P. E., Hall, P. J., Schilizzi, R. T., & Lazio, T. J. L. 2009, Proc. IEEE,

Dessart, L., Burrows, A., Ott, C. D., et al. 2006, ApJ, 644, 1063

Ding, H. 2022, PhD thesis, Swinburne University of Technology

97 (Piscataway, NJ: IEEE), 1482

862, 139

¹⁶ https://github.com/Phlya/adjustText

```
Ding, H., Deller, A., Lower, M., & Shannon, R. 2023a, IAU Symp. 363,
   Neutron Star Astrophysics at the Crossroads: Magnetars and the
   Multimessenger Revolution, 16 (Cambridge: Cambridge Univ. Press), 271
Ding, H., Deller, A. T., Fonseca, E., et al. 2021, ApJL, 921, L19
Ding, H., Deller, A. T., Freire, P., et al. 2020a, ApJ, 896, 85
Ding, H., Deller, A. T., Lower, M. E., et al. 2020b, MNRAS, 498, 3736
Ding, H., Deller, A. T., Stappers, B. W., et al. 2023b, MNRAS, 519, 4982
Doi, A., Fujisawa, K., Habe, A., et al. 2006, PASJ, 58, 777
Drout, M., Piro, A., Shappee, B., et al. 2017, Sci, 358, 1570
Eichler, D., Livio, M., Piran, T., & Schramm, D. N. 1989, Natur, 340, 126
Faulkner, A. J., Kramer, M., Lyne, A., et al. 2005, ApJL, 618, L119
Ferdman, R., Freire, P., Perera, B., et al. 2020, Natur, 583, 211
Ferdman, R. D., Stairs, I. H., Kramer, M., et al. 2014, MNRAS, 443, 2183
Flyamer, I., Xue, Z., Colin, et al. 2024, Phlya/adjustText: v1.1.1, Zenodo,
   doi:10.5281/zenodo.10835887
Fomalont, E. B., & Kopeikin, S. M. 2003, ApJ, 598, 704
Fong, W.-f., & Berger, E. 2013, ApJ, 776, 18
Fong, W.-f., Nugent, A. E., Dong, Y., et al. 2022, ApJ, 940, 56
Fonseca, E., Stairs, I. H., & Thorsett, S. E. 2014, ApJ, 787, 82
Fox, D. B., Frail, D. A., Price, P. A., et al. 2005, Natur, 437, 845
Fu, S. W., Weisz, D. R., Starkenburg, E., et al. 2023, ApJ, 958, 167
Gessner, A., & Janka, H.-T. 2018, ApJ, 865, 61
Giacobbo, N., & Mapelli, M. 2019, MNRAS, 482, 2234
Goldstein, A., Veres, P., Burns, E., et al. 2017, ApJL, 848, L14
Greisen, E. W. 2003, in Information Handling in Astronomy-Historical
   Vistas, ed. A. Heck (Dordrecht: Kluwer), 109
Han, J., Wang, C., Wang, P., et al. 2021, RAA, 21, 107
Han, Z., Podsiadlowski, P., & Eggleton, P. P. 1994, MNRAS, 270, 121
Haniewicz, H. T., Ferdman, R. D., Freire, P. C., et al. 2021, MNRAS,
   500, 4620
Hansen, T. T., Marshall, J. L., Simon, J., et al. 2020, ApJ, 897, 183
Hansen, T. T., Simon, J. D., Marshall, J. L., et al. 2017, ApJ, 838, 44
Harris, C. R., Millman, K. J., Van Der Walt, S. J., et al. 2020, Natur, 585, 357
Hartigan, J. A., & Hartigan, P. M. 1985, Ann. Statist., 13, 70
Hartigan, P. 1985, J. R. Stat. Soc. C Appl., 34, 320
Hulse, R. A., & Taylor, J. H. 1975, ApJL, 195, L51
Hunter, J. D. 2007, CSE, 9, 90
Jacoby, B. A., Cameron, P., Jenet, F., et al. 2006, ApJL, 644, L113
Ji, A. P., Frebel, A., Chiti, A., & Simon, J. D. 2016, Natur, 531, 610
Jones, S., Röpke, F. K., Pakmor, R., et al. 2016, A&A, 593, A72
Keane, E., Bhattacharyya, B., Kramer, M., et al. 2015, in Proc. Advancing
   Astrophysics with the Square Kilometre Array (AASKA14) (Trieste:
   SISSA), 40
Kettenis, M., van Langevelde, H. J., Reynolds, C., & Cotton, B. 2006, in ASP
   Conf. Ser. 351, Astronomical Data Analysis Software and Systems XV, ed.
   C. Gabriel et al., 497
Kirsten, F., Vlemmings, W., Freire, P., et al. 2014, A&A, 565, A43
Kitaura, F. S., Janka, H. T., & Hillebrandt, W. 2006, A&A, 450, 345
Knigge, C., Coe, M. J., & Podsiadlowski, P. 2011, Natur, 479, 372
Korobkin, O., Rosswog, S., Arcones, A., & Winteler, C. 2012, MNRAS,
   426, 1940
Kramer, M., Stairs, I., Manchester, R., et al. 2021a, PhRvX, 11, 041050
Kramer, M., Stairs, I., Venkatraman Krishnan, V., et al. 2021b, MNRAS,
   504, 2094
Kramer, M., Stairs, I. H., Manchester, R., et al. 2006, Sci, 314, 97
Leibler, C., & Berger, E. 2010, ApJ, 725, 1202
Li, D., & Pan, Z. 2016, RaSc, 51, 1060
Lynch, R. S., Boyles, J., Ransom, S. M., et al. 2013, ApJ, 763, 81
```

Lynch, R. S., Swiggum, J. K., Kondratiev, V. I., et al. 2018, ApJ, 859, 93

```
Manchester, R. N., Hobbs, G. B., Teoh, A., & Hobbs, M. 2005, AJ, 129, 1993
Martinez, J., Stovall, K., Freire, P., et al. 2015, ApJ, 812, 143
Martinez, J., Stovall, K., Freire, P., et al. 2017, ApJL, 851, L29
McKinnon, M., Beasley, A., Murphy, E., et al. 2019, BAAS, 51, 81
Miao, C., Zhu, W., Li, D., et al. 2023, MNRAS, 518, 1672
Middelberg, E., Deller, A. T., Norris, R. P., et al. 2013, A&A, 551, A97
Mooley, K., Deller, A., Gottlieb, O., et al. 2018, Natur, 561, 355
Müller, B., Tauris, T. M., Heger, A., et al. 2019, MNRAS, 484, 3307
Murphy, E., Bolatto, A., Chatterjee, S., et al. 2018, in ASP Conf. Ser. 517,
   Science with a Next Generation Very Large Array, 517, ed. E. Murphy (San
  Francisco, CA: ASP), 3
O'Connor, B., Troja, E., Dichiara, S., et al. 2022, MNRAS, 515, 4890
Pitkin, M. 2018, JOSS, 3, 538
Podsiadlowski, P., Dewi, J. D. M., Lesaffre, P., et al. 2005, MNRAS,
Podsiadlowski, P., Langer, N., Poelarends, A. J. T., et al. 2004, ApJ, 612, 1044
Possolo, A., Merkatas, C., & Bodnar, O. 2019, Metro, 56, 045009
Price, D. C., Flynn, C., & Deller, A. 2021, PASA, 38, e038
Radcliffe, J. F., Garrett, M. A., Beswick, R. J., et al. 2016, A&A, 587, A85
Rosen, R., Swiggum, J., McLaughlin, M., et al. 2013, ApJ, 768, 85
Safarzadeh, M., Ramirez-Ruiz, E., Andrews, J. J., et al. 2019, ApJ, 872,
Sengar, R., Balakrishnan, V., Stevenson, S., et al. 2022, MNRAS, 512, 5782
Shklovskii, I. S. 1970, SvA, 13, 562
Siess, L., & Lebreuilly, U. 2018, A&A, 614, A99
Simon, J. D., & Geha, M. 2007, ApJ, 670, 313
Sokolovsky, K. V., Kovalev, Y. Y., Pushkarev, A. B., & Lobanov, A. P. 2011,
  A&A. 532, A38
Stairs, I. H., Thorsett, S. E., Taylor, J. H., & Wolszczan, A. 2002, ApJ,
  581, 501
Stovall, K., Freire, P., Chatterjee, S., et al. 2018, ApJL, 854, L22
Stovall, K., Lynch, R., Ransom, S., et al. 2014, ApJ, 791, 67
Swiggum, J. K., Rosen, R., McLaughlin, M., et al. 2015, ApJ, 805, 156
Tan, C. M., Fonseca, E., Crowter, K., et al. 2024, ApJ, 966, 26
Tauris, T. M., & Bailes, M. 1996, A&A, 315, 432
Tauris, T. M., & Janka, H.-T. 2019, ApJL, 886, L20
Tauris, T. M., Kramer, M., Freire, P. C. C., et al. 2017, ApJ, 846, 170
Tauris, T. M., Langer, N., Moriya, T. J., et al. 2013, ApJL, 778, L23
Tauris, T. M., Langer, N., & Podsiadlowski, P. 2015, MNRAS, 451, 2123
Tauris, T. M., & van den Heuvel, E. P. J. 2023, Physics of Binary Star
  Evolution. From Stars to X-ray Binaries and Gravitational Wave Sources
  (Princeton, NJ: Princeton Univ. Press)
Tunnicliffe, R., Levan, A., Tanvir, N., et al. 2014, MNRAS, 437, 1495
Verbunt, F., Igoshev, A., & Cator, E. 2017, A&A, 608, A57
Vigna-Gómez, A., Neijssel, C. J., Stevenson, S., et al. 2018, MNRAS,
  481, 4009
Virtanen, P., Gommers, R., Oliphant, T. E., et al. 2020, NatMe, 17, 261
Voitsik, P., Pushkarev, A., Kovalev, Y. Y., et al. 2018, ARep, 62, 787
Voss, R., & Tauris, T. M. 2003, MNRAS, 342, 1169
Watson, D., Hansen, C. J., Selsing, J., et al. 2019, Natur, 574, 497
Weisberg, J. M., & Huang, Y. 2016, ApJ, 829, 55
Weisz, D. R., Dolphin, A. E., Skillman, E. D., et al. 2014, ApJ, 789, 148
Wex, N. 2014, in Brumberg Festschrift, ed. S. M. Kopeikein (Berlin: De
  Gruyter)
Wong, T.-W., Willems, B., & Kalogera, V. 2010, ApJ, 721, 1689
Yao, J. M., Manchester, R. N., & Wang, N. 2017, ApJ, 835, 29
Zevin, M., Kremer, K., Siegel, D. M., et al. 2019, ApJ, 886, 4
Zevin, M., Nugent, A. E., Adhikari, S., et al. 2022, ApJL, 940, L18
Zhu, W., Desvignes, G., Wex, N., et al. 2019, MNRAS, 482, 3249
```